Electronic Supplementary Material (ESI) for Journal of Materials Chemistry A.
This journal is © The Royal Society of Chemistry 2024

Copper Shape-Templated N-Doped Carbons: Exercising Selective Surface Area Control for Lithium-Ion Batteries & Beyond

Supporting Information

Samantha N. Lauro,[a] *James N. Burrow,*[b] *Benjamin G. Broekhuis,*[b] *Philippe Papa,*[a,b] *and C. Buddie Mullins*[*,a,b,c]

a Department of Chemistry, The University of Texas at Austin, Austin, Texas 78712-1224, United States.

b McKetta Department of Chemical Engineering, The University of Texas at Austin, Austin, Texas 78712-1589, United States.

c Texas Materials Institute, The University of Texas at Austin, Austin, Texas 78712-1591, United States.

Table of Contents

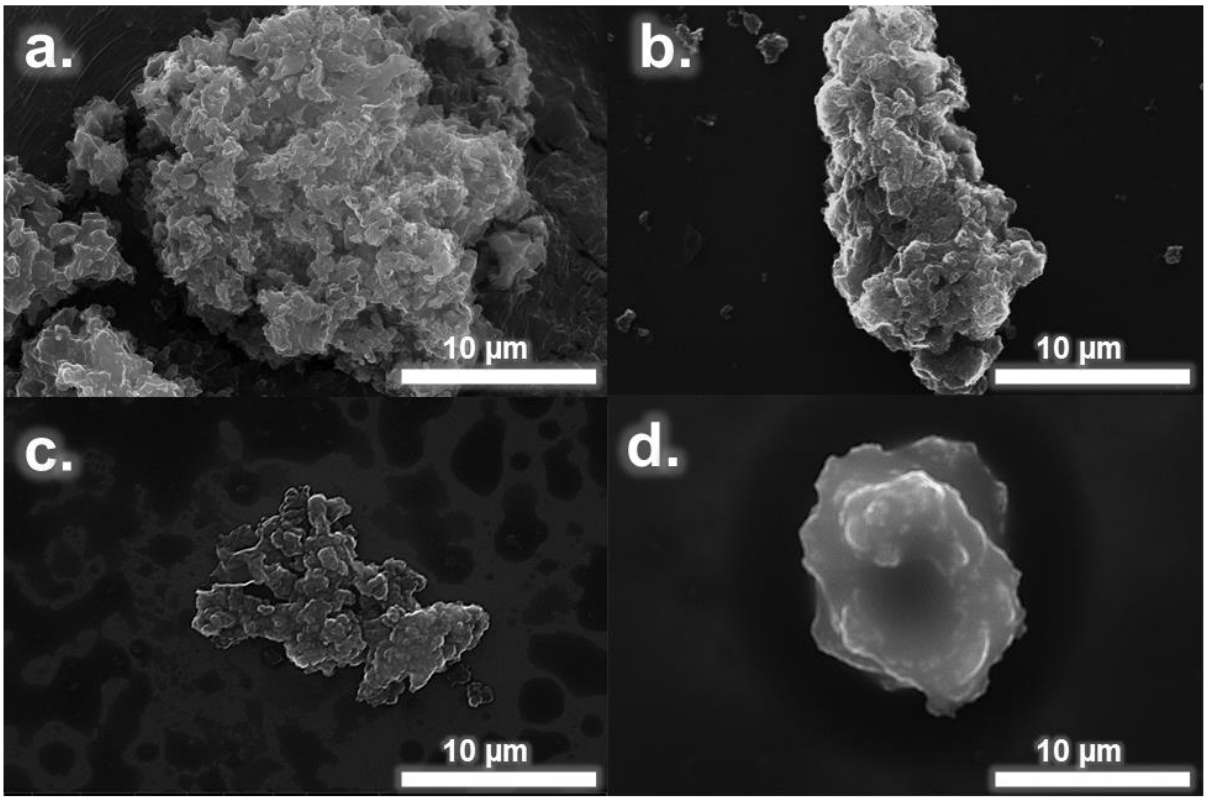

Figure S1. Additional zoomed-in SEM images of g-C_3N_4 precursor (**a**), dendritic templated N-doped carbon (**b**), flake templated N-doped carbon (**c**), and spheroidal templated N-doped carbon (**d**).

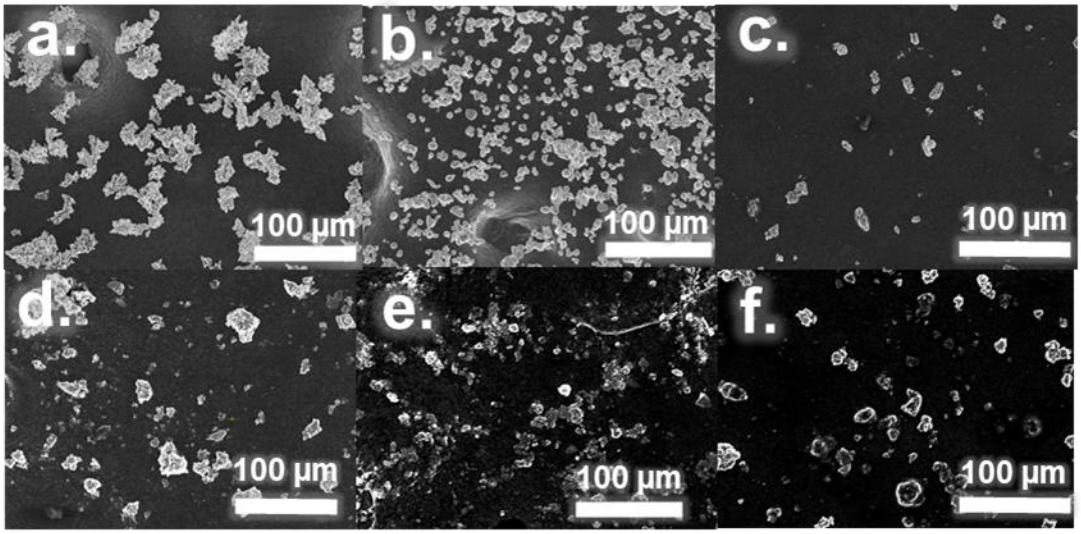

Figure S2. SEM images of population of dendritic copper (**a**), spheroidal copper (**b**), flake copper (**c**), dendritic-copper templated N-doped carbons (**d**), spheroidal-copper templated N-doped carbons (**e**), and flake-copper templated N-doped carbons (**f**).

For analysis of the XRD patterns:

The d-spacing (d) was determined by using the Bragg equation:

$2\mathrm{d}\ \sin\theta = \mathrm{n}\lambda$

where:

n is a positive integer

λ is the x-ray wavelength (1.5418 Å)

θ is the Bragg angle in radians

The crystallite size (L_c and L_a) was determined by using the Scherrer equation:

$$L = \frac{K\lambda}{\beta \cos\theta}$$

where:

L is the average crystallite size

λ is the x-ray wavelength (1.5418 Å)

K is the shape parameter (0.89 for L_c and 1.84 for L_a)

β is the FWHM in radians

θ is the Bragg angle in radians

Table S1. Estimated Crystallite Parameters of N-Doped Carbons from XRD

Sample	L_c (Å)	d_{002} (Å)	002 # of sheets	L_a (Å)	d_{101} (Å)	101 # of repeats
Dendritic	11.14	3.36	3.31	8.71	4.29	2.03
Spheroidal	10.13	3.40	2.97	6.98	4.26	1.64
Flake	10.76	3.41	3.15	6.45	4.19	1.54

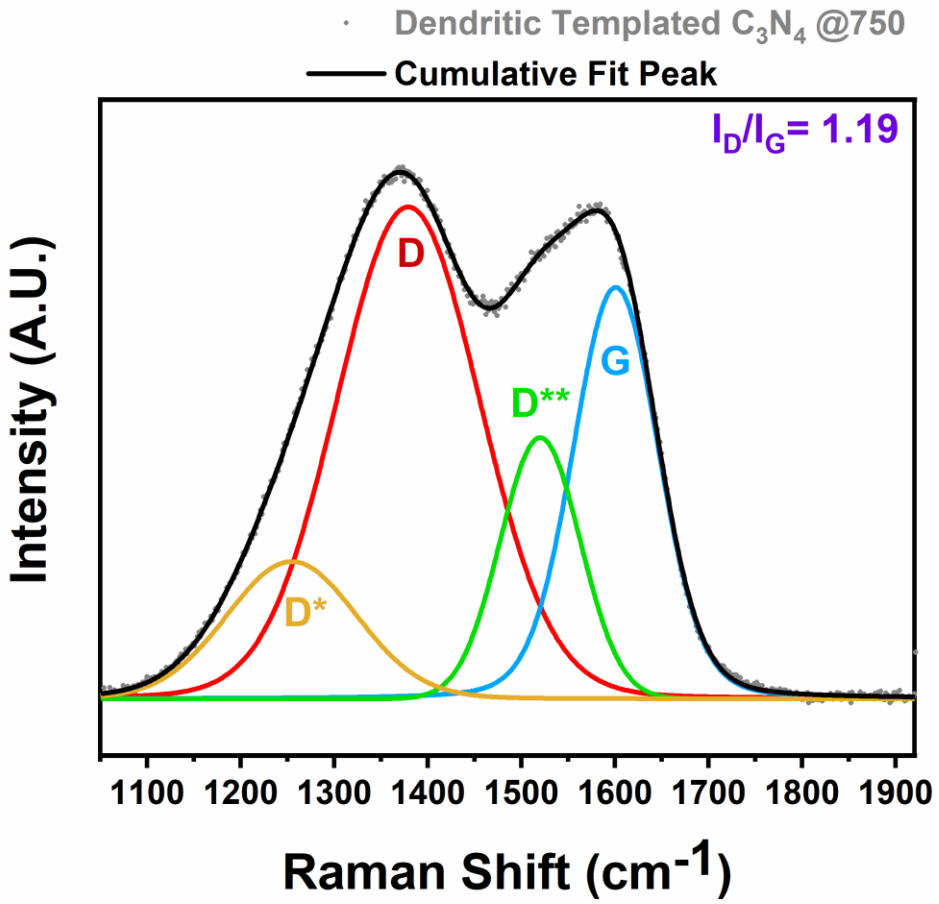

Figure S3. Example of Raman spectra fitting to determine the I_D/I_G ratio. Spectra were fit with four peaks representing the D^*, D, D^{**}, and G band.

Table S2. Raman Fitting Parameters for N-Doped Carbons

Sample	D*	D	D**	G	I_D/I_G
Dendritic	1254.6 cm^{-1}	1379.1 cm^{-1}	1520.0 cm^{-1}	1600.8 cm^{-1}	1.19
Spheroidal	1219.6 cm^{-1}	1365.5 cm^{-1}	1501.6 cm^{-1}	1588.6 cm^{-1}	1.19
Flake	1241.1 cm^{-1}	1366.1 cm^{-1}	1505.8 cm^{-1}	1591.9 cm^{-1}	1.20

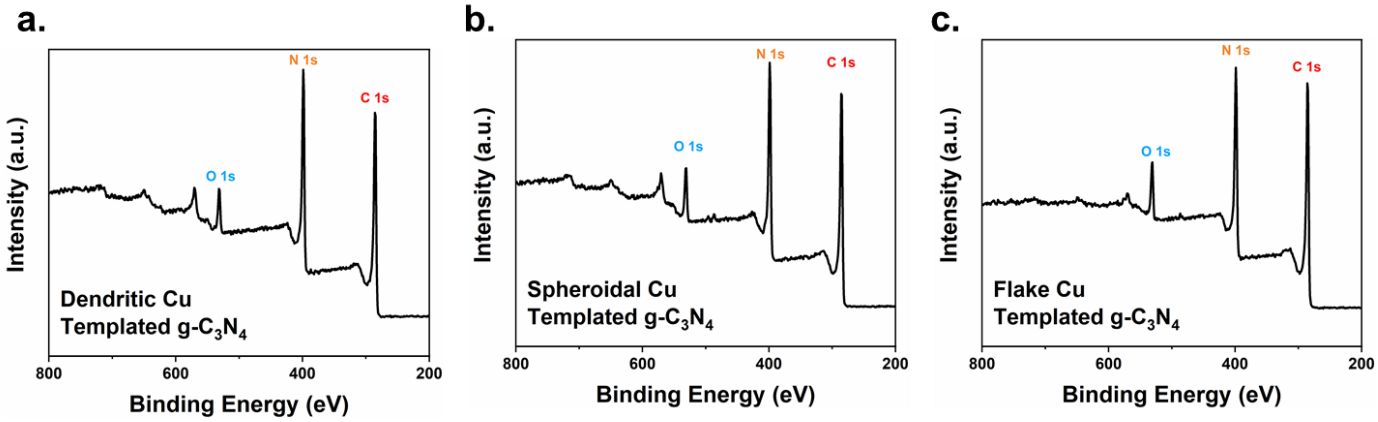

Figure S4. XPS survey scans of dendritic (**a**) spheroidal (**b**) and flake(**c**) templated carbons.

Table S3. XPS Elemental Composition of N-Doped Carbons

Sample	% Carbon	% Nitrogen	% Oxygen	% Copper
Dendritic	62.6	31.2	4.9	1.4
Spheroidal	62.9	30.2	5.8	1.2
Flake	63.7	31.0	5.1	0.3

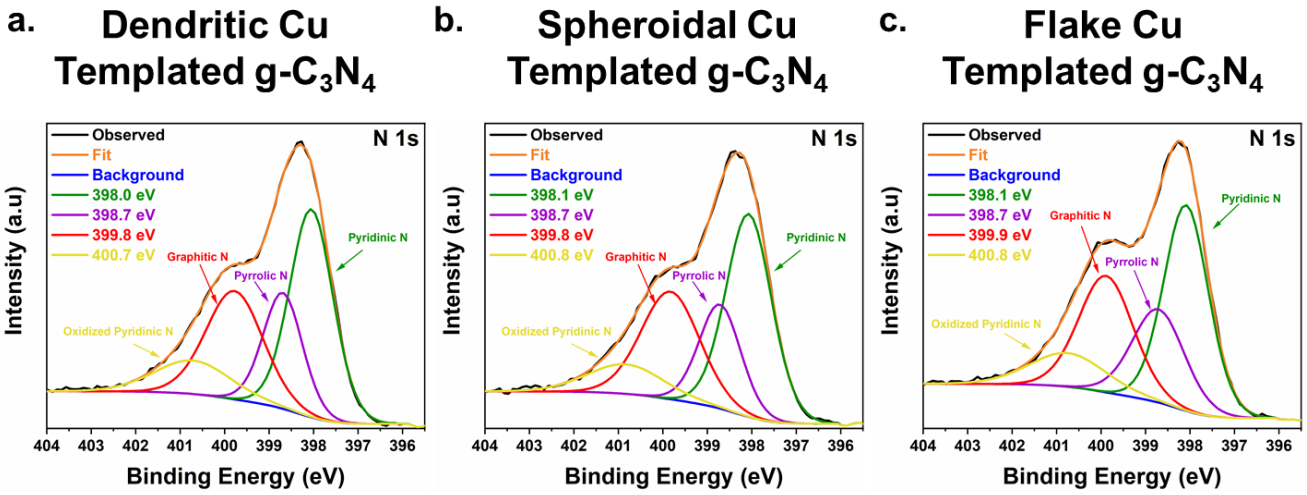

Figure S5. XPS N1s region scans of dendritic (**a**) spheroidal (**b**) and flake(**c**) templated carbons.

Table S4. XPS Nitrogen Composition of N-Doped Carbons

Sample	Fractional % Pyridinic N	Fractional % Pyrrolic N	Fractional % Graphitic N	Fractional % Oxidized N
Dendritic	40.4	20.5	27.8	11.3
Spheroidal	41.8	19.7	28.4	10.1
Flake	40.1	21.2	27.6	11.1

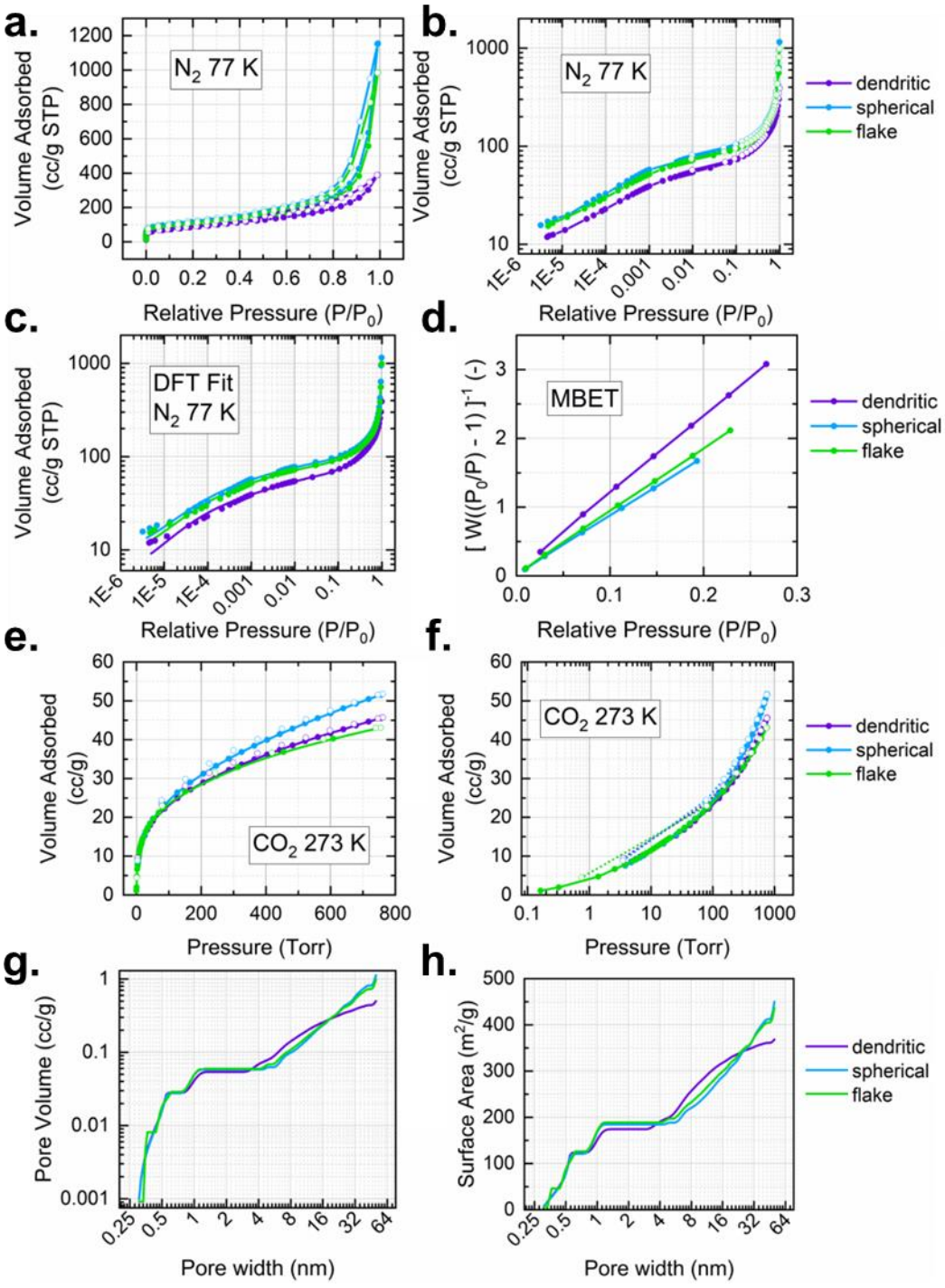

Figure S6. Gas adsorption isotherms employed for porosimetry. **a-c**) N_2 isotherms at 77 K plotted over linear (**a**) and logarithmic (**b**) scales, and DFT fits (**c**). Multi-point BET analysis of N_2 adsorption employed for surface area quantification (**d**).CO_2 isotherms at 273 K to quantify ultramicroporosity, plotted over linear (**e**) and logarithmic (**f**) scale. Pore volume (**g**) and surface area (**h**) distributions.

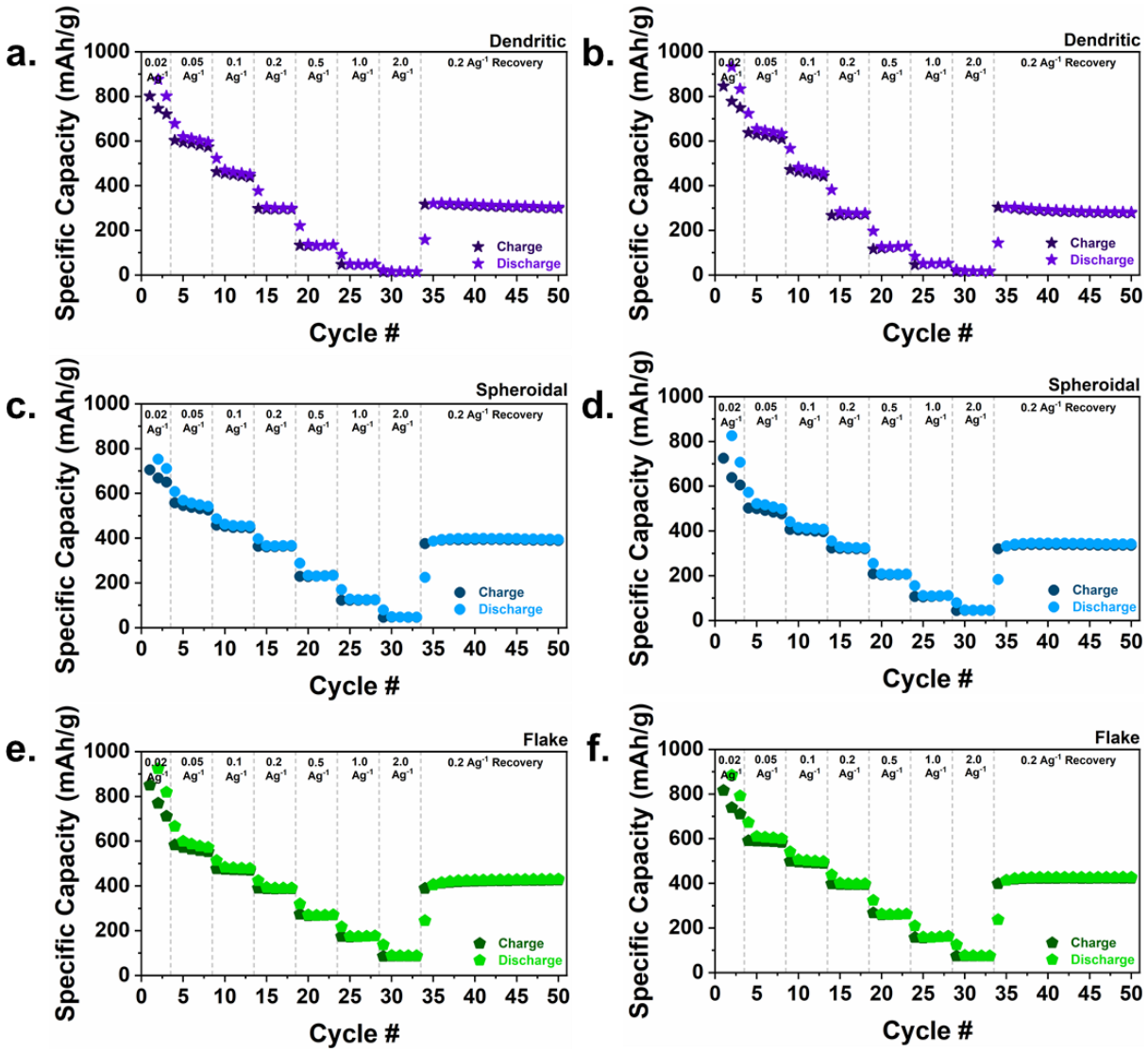

Figure S7. Variable rate cycling of duplicate cells for dendritic (**a**, **b**), spheroidal (**c**, **d**), and flake (**e**, **f**) templated carbons.

Table S5. Average Capacity for Variable Rate Cycling

Sample	Capacity at 0.05 A g^{-1} (mAh g^{-1})	Capacity at 0.1 A g^{-1} (mAh g^{-1})	Capacity at 0.2 A g^{-1} (mAh g^{-1})	Capacity at 0.5 A g^{-1} (mAh g^{-1})	Capacity at 1.0 A g^{-1} (mAh g^{-1})	Capacity at 2.0 A g^{-1} (mAh g^{-1})
Dendritic	640 ± 4%	481 ± 3%	308 ± 4%	146 ± 5%	58 ± 1%	17 ± 8%
Spheroidal	544 ± 5%	440 ± 7%	352 ± 8%	230 ± 8%	127 ± 9%	54 ± 1%
Flake	610 ± 2%	498 ± 3%	403 ± 2%	277 ± 2%	177 ± 6%	92 ± 10%

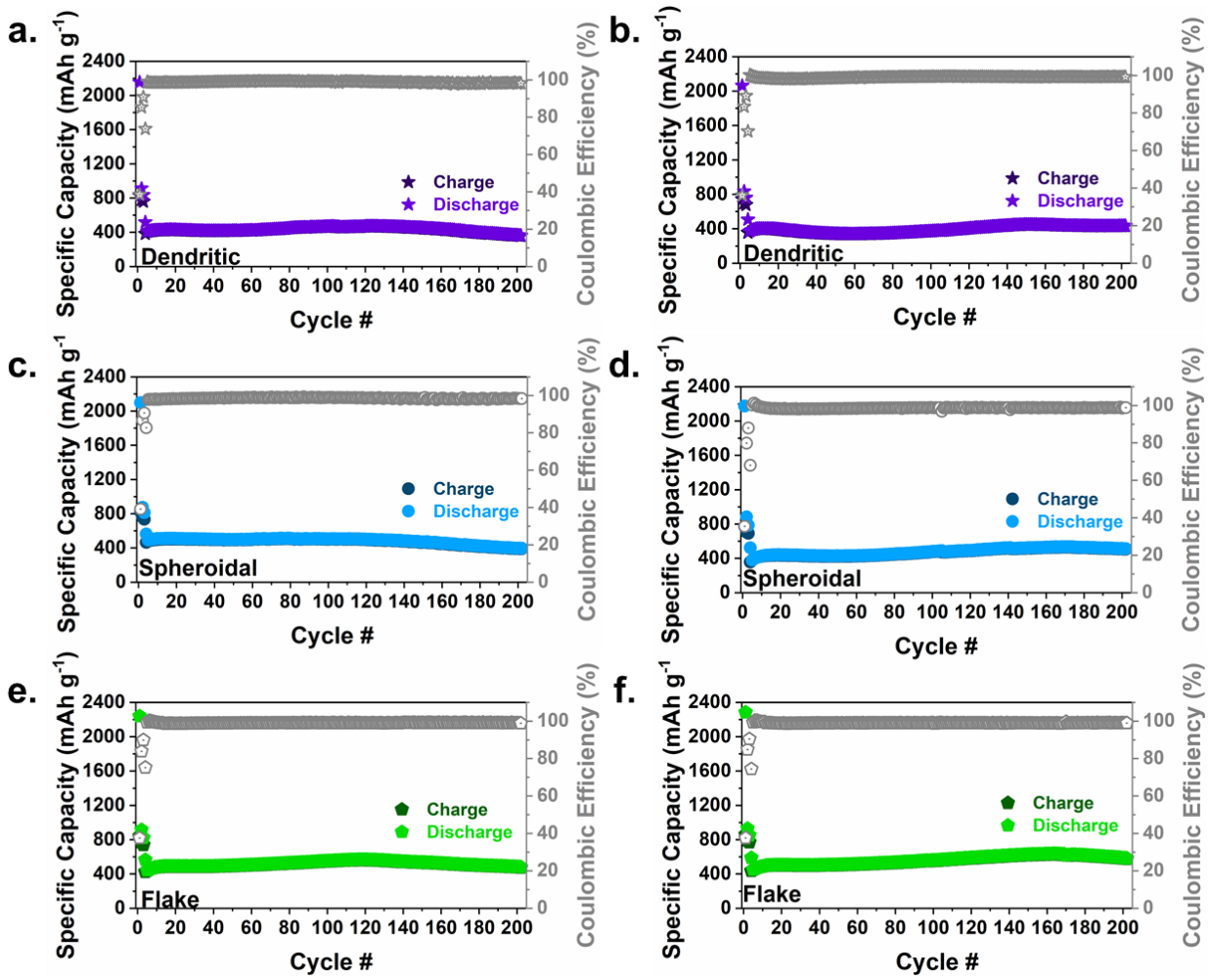

Figure S8. Long-term cycling at 0.2 A g^{-1} with three formation cycles at 0.02 A g^{-1} of duplicate cells for dendritic (**a**, **b**), spheroidal (**c**, **d**), and flake (**e**, **f**) templated carbons. It should be noted that the cells represented in (**a,c,e**) were cycled at the same time, and cells represented in (**b,d,f**) were cycled together but at a separate time from (**a,c,e**). Slight differences in the room temperature during these time periods correlates to the change in curve shape between the two sample sets.

Table S6. Average Capacity and Coulombic Efficiency for Long-term Cycling

Sample	Average Capacity ($mAh\ g^{-1}$)	Average Coulombic Efficiency (%)
Dendritic	416 ± 6%	98.8± 0.1
Spheroidal	483± 1%	98.9± 0.2
Flake	541± 6%	98.9± 0.1

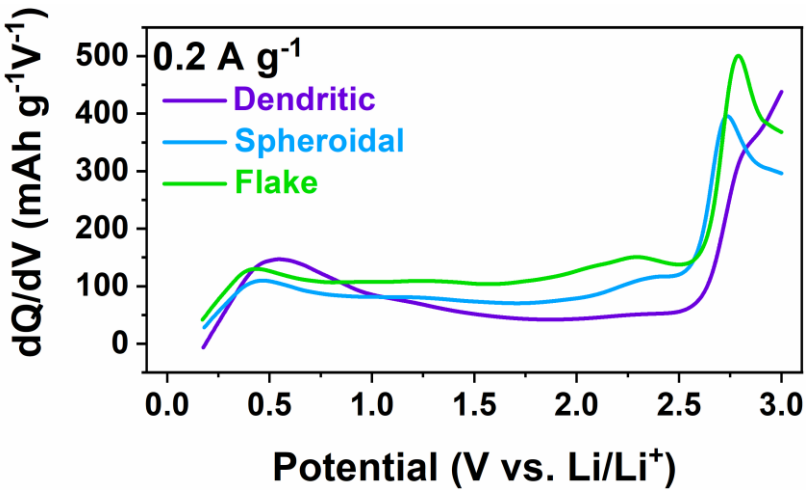

Figure S9. Absolute dQ dV^{-1} curve of flake, spheroidal and dendritic N-doped carbons of lithium extraction at a cycling rate of 0.2 A g^{-1}.

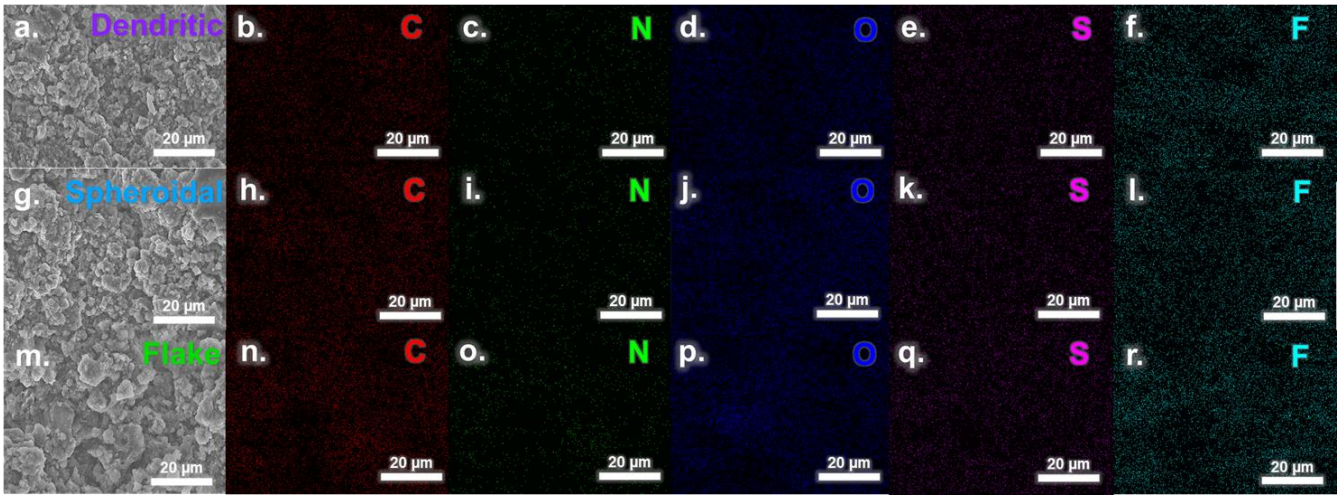

Figure S10. Post-mortem analysis of cycled carbon electrodes. SEM image of cycled dendritic N-doped carbon electrode (**a**) and corresponding EDX of carbon (**b**), nitrogen (**c**), oxygen (**d**), sulfur (**e**), and fluorine (**f**) signal in SEI. SEM image of cycled spheroidal N-doped carbon electrode (**g**) and corresponding EDX of carbon (**h**), nitrogen (**i**), oxygen (**j**), sulfur (**k**), and fluorine (**l**) signal in SEI. SEM image of cycled flake N-doped carbon electrode (**m**) and corresponding EDX of carbon (**n**), nitrogen (**o**), oxygen (**p**), sulfur (**q**), and fluorine (**r**) signal in SEI.

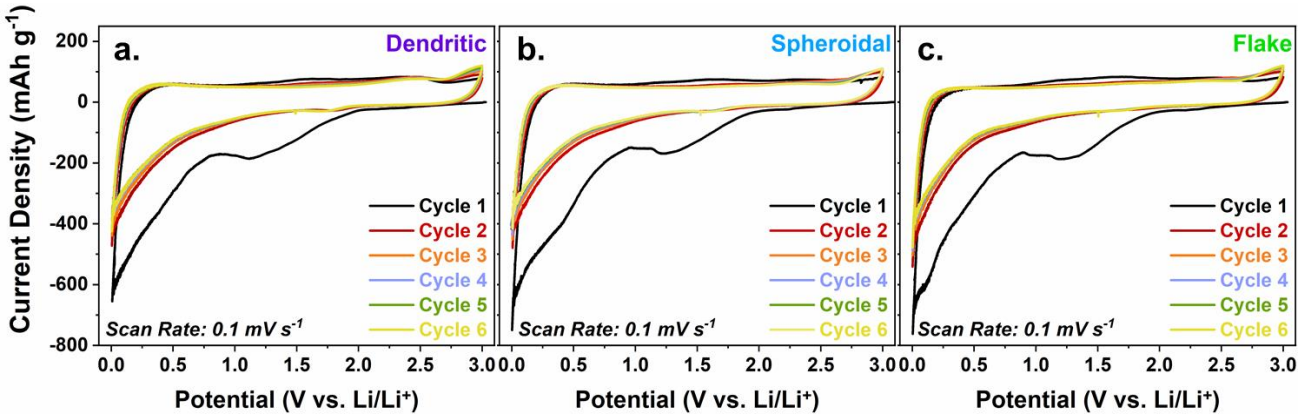

Figure S11. Cyclic voltammograms at a scan rate of 0.1 mV s^{-1} of dendritic (**a**), spheroidal (**b**), and flake (**c**) templated carbons.

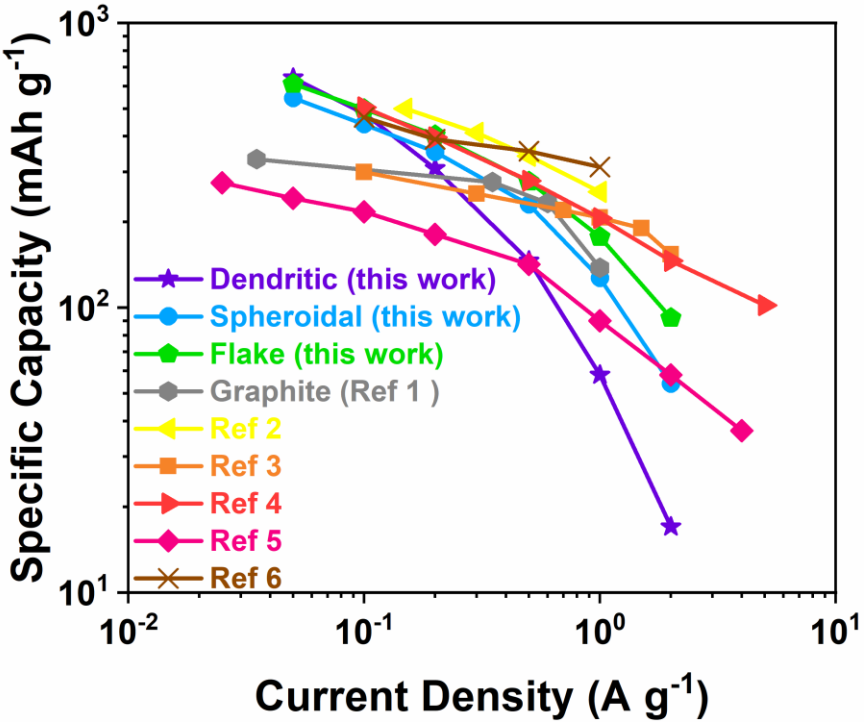

Figure S12. Comparative plot of dendritic, spheroidal, and flake carbons from this work compared to graphite,[1] and previous reported N-doped carbon microspheres,[2] protein derived N-doped carbon,[3] covalent-organic framework derived N-doped carbon,[4] garlic-peel derived N-doped carbon,[5] and N-doped carbon nanotubes.[6]

References

(1) Jang, D.; Suh, S.; Yoon, H.; Kim, J.; Kim, H.; Baek, J.; Kim, H.-J. Enhancing Rate Capability of Graphite Anodes for Lithium-Ion Batteries by Pore-Structuring. *Applied Surface Science Advances* **2021**, *6*, 100168. https://doi.org/10.1016/j.apsadv.2021.100168.

(2) Chen, T.; Pan, L.; J. Loh, T. A.; C. Chua, D. H.; Yao, Y.; Chen, Q.; Li, D.; Qin, W.; Sun, Z. Porous Nitrogen-Doped Carbon Microspheres as Anode Materials for Lithium Ion Batteries. *Dalton Transactions* **2014**, *43* (40), 14931–14935. https://doi.org/10.1039/C4DT01223B.

(3) An, G.-H.; Kim, H.; Ahn, H.-J. Surface Functionalization of Nitrogen-Doped Carbon Derived from Protein as Anode Material for Lithium Storage. *Applied Surface Science* **2019**, *463*, 18–26. https://doi.org/10.1016/j.apsusc.2018.08.201.

(4) Zhang, X.; Zhu, G.; Wang, M.; Li, J.; Lu, T.; Pan, L. Covalent-Organic-Frameworks Derived N-Doped Porous Carbon Materials as Anode for Superior Long-Life Cycling Lithium and Sodium Ion Batteries. *Carbon* **2017**, *116*, 686–694. https://doi.org/10.1016/j.carbon.2017.02.057.

(5) Selvamani, V.; Ravikumar, R.; Suryanarayanan, V.; Velayutham, D.; Gopukumar, S. Garlic Peel Derived High Capacity Hierarchical N-Doped Porous Carbon Anode for Sodium/Lithium Ion Cell. *Electrochimica Acta* **2016**, *190*, 337–345. https://doi.org/10.1016/j.electacta.2016.01.006.

(6) Li, J.; Zhang, F.; Wang, C.; Shao, C.; Li, B.; Li, Y.; Wu, Q.-H.; Yang, Y. Self Nitrogen-Doped Carbon Nanotubes as Anode Materials for High Capacity and Cycling Stability Lithium-Ion Batteries. *Materials & Design* **2017**, *133*, 169–175. https://doi.org/10.1016/j.matdes.2017.07.060.